REDUCTION OF ATMOSPHERIC WATER VAPOUR EFFECTS ON ENVISAT ASAR INTERFEROGRAMS USING MERIS NEAR IR MEASUREMENTS

Zhenhong Li

Department of Civil, Environmental and Geomatic Engineering, University College London, London WC1E 6BT, UK
Now at Department of Geographical and Earth Sciences, University of Glasgow, Glasgow G12 8QQ, UK
Zhenhong.Li@ges.gla.ac.uk

Commission VII, WG VII/2

KEY WORDS: SAR, Change Detection, Radar, Integration, Monitoring, Mapping, Surface, Geodesy

ABSTRACT:

Atmospheric water vapour effects represent a major limitation of repeat-pass Interferometric SAR (InSAR) techniques including InSAR time series approaches (e.g. permanent scatterers (PS) and small baseline subset (SBAS)). In this paper, it is demonstrated that atmospheric water vapour effects greater than 4 cm can be observed even in desert regions (e.g. Southern California) and the use of MERIS correction model can improve the accuracy of InSAR derived deformation signals from 9.9 mm to 4.1 mm. It is also shown that, using an advanced integration technique titled InSAR Time Series with Water Vapour correction model (InSAR TS + PWV) for reduction of water vapour effects with coincident MERIS near IR water vapour data, a time series of postseismic motion after the 2003 Bam (Iran) earthquake is achievable with about 50% reduction in RMS model misfit. It is believed that this study not only contributes directly to the ENVISAT mission, but also will benefit space agencies' plans to design and launch InSAR missions because it aids in the identification of necessary characteristics of their future InSAR missions.

1. INTRODUCTION

Land surface deformation is a major worldwide hazard which can result from natural processes such as earthquakes, volcanoes and landslides, or from anthropogenic processes including extraction of groundwater, oil and coal. Surface displacement causes many problems including economic loss and human suffering. One estimate placed the direct annual cost of subsidence damage and mitigation within the USA alone at over $100 million (Panel on Land Subsidence, 1991). Indirect costs of subsidence are even greater, such as the indication that subsidence was a contributing factor to the levee failures in New Orleans when hurricane Katrina hit in 2005 (Dixon et al., 2006). On 8 October 2005 one of the deadliest earthquakes in modern times struck the region of Kashmir in South Asia and claimed 80,000+ lives. Therefore, land deformation mapping is of crucial importance not only for sustainable economic development but also for the safety of the general public.

Interferometric SAR (InSAR) has been already revolutionizing our ability to image surface deformation at spatial resolutions of a few tens of metres in the last two decades, which in turn has led to many new insights into geophysical processes, such as earthquakes, volcanoes and landslides (Massonnet and Feigl, 1998). It is well-known that InSAR techniques are limited by atmospheric effects: any difference in radar signal propagation delays between SAR acquisitions leads to additional shifts in phase measurements, which largely result from changes in water vapour content in the troposphere (Hanssen, 2001). ESA's ENVISAT provides a unique opportunity to investigate atmospheric water vapour effects on SAR interferograms due to its two main payloads, Advanced Synthetic Aperture Radar (ASAR) and MEdium Resolution Imaging Spectrometer (MERIS): (1) There is no time difference between acquisitions of water vapour and SAR data; (2) MERIS full-resolution mode

has a high spatial resolution of up to 300 m; (3) MERIS and ASAR have a virtually identical propagation path.

2. ATMOSPHERIC EFFECTS ON INTERFEROGRAMS

2.1 Atmospheric Effects on Interferograms - Theory

After removing the flat earth and local topography, the unwrapped differential interferometric phase at pixel (x, r) computed from the SAR acquisitions at times t_M, the start time, and t_S, the end time, can be written as follows (Berardino et al., 2002):

$$
\begin{cases}
\delta\phi_{t_M t_S}(x,r) = \delta\phi_{t_M t_S}^{topo}(x,r) + \delta\phi_{t_M t_S}^{disp}(x,r) + \delta\phi_{t_M t_S}^{atm}(x,r) + \delta\phi_{t_M t_S}^{noise}(x,r) \\
\delta\phi_{t_M t_S}^{topo}(x,r) = \dfrac{4\pi}{\lambda} \dfrac{B_{\perp t_M t_S} \Delta Z(x,r)}{r\sin\theta} \\
\delta\phi_{t_M t_S}^{disp}(x,r) = \dfrac{4\pi}{\lambda} \left[d(t_S, x, r) - d(t_M, x, r) \right] \\
\delta\phi_{t_M t_S}^{atm}(x,r) = \dfrac{4\pi}{\lambda} \left[d_{atm}(t_S, x, r) - d_{atm}(t_M, x, r) \right]
\end{cases}
\tag{1}
$$

where λ is the transmitted signal central wavelength (in mm, e.g. c. 56.3 mm for ASAR), $d(t_S, x, r)$ and $d(t_M, x, r)$ represent the cumulative deformation in the line of sight at times t_S and t_M respectively, with respect to the reference instant t_0, i.e., implying $d(t_0, x, r) = 0, \forall(x, r)$; $\Delta Z(x, r)$ is topographic error present in the DEM used for interferogram generation, and its impact on deformation maps is also a function of the perpendicular baseline component $B_{\perp t_M t_S}$, the sensor-target distance r, and the look angle θ. The terms $d_{atm}(t_M, x, r)$ and $d_{atm}(t_S, x, r)$ account for temporal

atmospheric variations at pixel (x, r), and the last term $\delta\phi^{noise}_{t_M t_S}(x, r)$ for temporal decorrelation, orbital errors and thermal noise effects.

In Equation (1), it is clear that the smaller the perpendicular baseline, the less the impact of DEM errors on a deformation map. Assuming a nominal incidence angle of 23° and a perpendicular baseline of 100 m, the typical topographic errors in the SRTM DEM (c. 8.7m in Eurasia (Farr et al., 2007)) might lead to a phase error of 0.61 rad, which is well below the typical phase noise level of the InSAR pairs, on the order of ~0.70 rad (Hanssen, 2001). Therefore, the topographic contribution can be considered negligible for InSAR pairs with a perpendicular baseline of 100 m or shorter.

Atmospheric effects were first identified in repeat-pass InSAR measurements by (Massonnet et al., 1994) when they studied the 1992 Landers earthquake. Zebker et al. (1997) suggested that a 20% spatial or temporal change in relative humidity could result in a 10-14 cm error in deformation measurement retrievals, independent of baseline parameter. It should be noted that the atmospheric phase component in Equation (1) also includes ionospheric effects (Hanssen, 2001). However, because the occurrence of phase scintillation due to small-scale ionospheric disturbances is limited in the equatorial and auroral regions, and extremely rare in mid-latitude regions; and ionospheric effects on InSAR measurements should be ~17 times less at C-band than at L-band, an assumption is made in this paper that ionospheric effects will not significantly affect phase variations in C-band SAR images, although they may lead to long wavelength gradients which can be removed using a best-fit plane (Massonnet and Feigl, 1998).

3. MERIS WATER VAPOUR CORRECTION MODEL FOR A SINGLE INTERFEROGRAM

3.1 MERIS near IR water vapour product

The MEdium Resolution Imaging Spectrometer (MERIS) was launched together with the Advanced Synthetic Aperture Radar (ASAR) on the ESA ENVISAT spacecraft on 1 March 2002. MERIS is a push-broom passive imaging instrument and measures the solar radiation reflected from the Earth's surface and clouds in the visible and near IR spectral range during the daytime with a swath width of 1150 km for the entire 68.5° field of view (ESA, 2004). MERIS uses two out of fifteen narrow spectral channels in the near IR for the remote sensing of Precipitable Water Vapour (PWV) either above land or ocean surfaces under cloud free conditions (Bennartz and Fischer, 2001) or above the highest cloud level under cloudy conditions (Albert et al., 2001). The wavelengths of these near IR channels have been chosen by the MERIS science team to minimize the effects of different spectral slopes of the surface. The two channels (i.e. channel 14: 885 nm and channel 15: 900 nm) are only 15 nm apart and spectral variations of surface reflectance are generally small (Bennartz and Fischer, 2001). In order to further minimize the spectral surface effect, a simple correction algorithm based on the ratio between MERIS channel 10 (753.75 nm) and channel 14 (885 nm) has been implemented in the ESA MERIS water vapour retrieval algorithm (Fischer and Bennartz, 1997). MERIS near IR water vapour products are available at two nominal spatial resolutions: 0.3 km for full resolution (FR) mode, and 1.2 km for reduced resolution (RR) mode.

Only measurements with wavelengths between 0.4 μm and 0.9 μm are used in the MERIS cloud mask algorithm to estimate whether a pixel is cloudy or not, and very valuable thermal information and information on liquid and ice water absorption at 1.6μm and 3μm are not available, therefore the MERIS cloud mask is not 'perfect', particularly in mountainous areas. A 'conservative' cloud mask using the relationship between surface pressure and topography can detect and mask out thin clouds to obtain better water vapour than those obtained using the ESA standard product (Li et al., 2006a; Ramon et al., 2003). Spatio-temporal comparisons show c. 1.1 mm agreement between MERIS and GPS/radiosonde water vapour products in terms of standard deviations (Li et al., 2006b).

3.2 MERIS water vapour correction

When MERIS water vapour data collected at times t_S and t_M are available, Zenith Path Delay Difference Maps (ZPDDM) can be derived as follows: In step 1, MERIS-PWV needs to be converted into Zenith Wet Delay (ZWD) using surface temperature measurements, which were obtained from radiosonde data in this study; In step 2, a ZPDDM is calculated by differencing two 2D ZWD fields (i.e. $ZPDDM = ZWD_2 - ZWD_1$); In step 3, an improved inverse distance weighted interpolation method (IIDW) (Li, 2004) can be applied to fill in the missing pixels due to the presence of clouds and/or problematic reflectance values; In step 4, to suppress the inherent noise of MERIS-PWV, a low-pass filter can be applied to the ZPDDM with an average width of c. 0.6 km for FR MERIS data and c. 2.4 km for RR MERIS data. Assuming pixel to pixel PWV errors are uncorrelated, the accuracy of the ZPDDM increases by a factor of 2 at the expense of the spatial resolution.
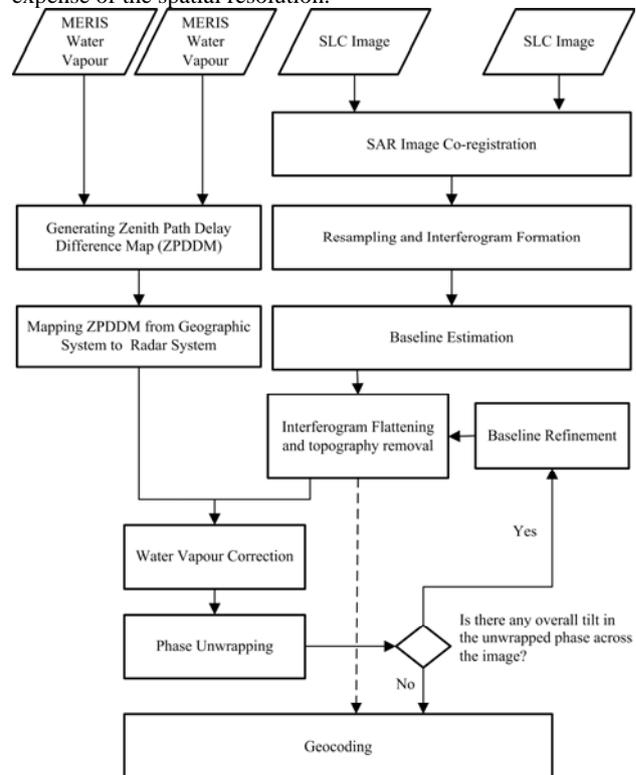
Figure 1. Two-pass differential InSAR processing flowchart with MERIS water vapour correction.

As shown in Figure 1, to reduce water vapour effects on the interferograms, ZPDDM are inserted into the interferometric processing sequence after removal of topographic signals by use of a precise DEM such as that produced by the Space Shuttle Radar Topography Mission (SRTM) (Farr et al., 2007); The procedure used for InSAR water vapour correction has been successfully incorporated into the JPL/Caltech ROI_PAC software by introducing two processing parameters: ACM_MODEL and ACM_IS_ZPDDM. ACM_MODEL can be set to NULL if no correction is applied; otherwise, the value ACM_IS_ZPDDM is used to distinguish the type of difference map(s) (currently, 0 = Slant Path Delay Difference Map (SPDDM), 1 = ZPDDM).

After water vapour correction, atmospheric effects on the corrected interferograms are limited and their residuals can be considered as random noise, so that $\delta\phi_{t_M t_S}^{atm}(x,r) = ZPDDM + \delta\phi_{t_M t_S}^{residual}(x,r)$ can be cancelled out in Equation (1):

$$\begin{cases} \delta\phi_{t_M t_S}^{corr}(x,r) = \delta\phi_{t_M t_S}^{topo}(x,r) + \delta\phi_{t_M t_S}^{disp}(x,r) + \delta\phi_{t_M t_S}^{noise^2}(x,r) \\ \qquad \delta\phi_{t_M t_S}^{corr}(x,r) = \delta\phi_{t_M t_S}(x,r) - ZPDDM \\ \delta\phi_{t_M t_S}^{noise^2}(x,r) = \delta\phi_{t_M t_S}^{noise}(x,r) + \delta\phi_{t_M t_S}^{residual}(x,r) \end{cases} \quad (2)$$

where $\delta\phi_{t_M t_S}^{corr}(x,r)$ represents corrected phase values and $\delta\phi_{t_M t_S}^{residual}(x,r)$ residual water vapour effects after correction.

3.3 To what extent can water vapour effects be reduced using MERIS?

−118°30′ −118°00′ −117°30′   −118°30′ −118°00′ −117°30′ −117°00′
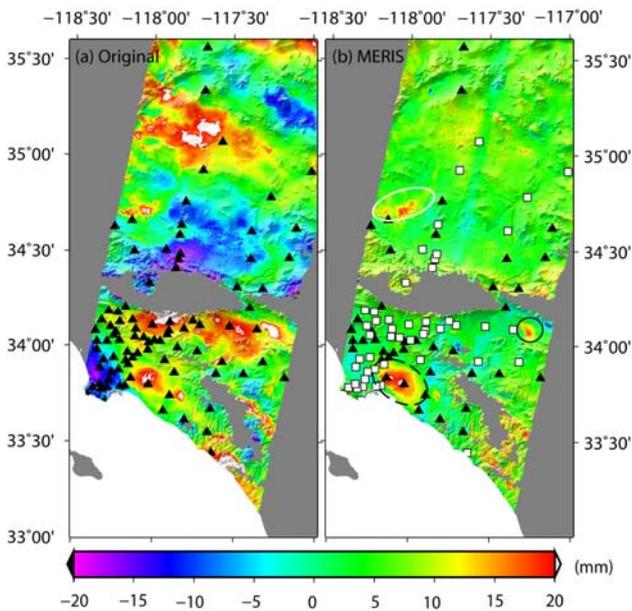
Figure 2. Interferogram (050514-050827) superimposed on a SRTM DEM. (a) Original interferogram; (b) Corrected interferogram using MERIS data. Note: (1) Grey within interferogram coverage implies areas with low coherence due to steep slopes and vegetation; (2) Negative values imply that the surface moves towards the satellite; (3) In Figure 2(b), black

solid triangles represent GPS stations where the agreements of InSAR-derived and GPS-derived range changes are within a 1-sigma range both before and after correction, white squares with black borders imply improvement in their agreements after correction, and red solid circles indicate deterioration in their agreements after correction; (4) The circle and ovals in Figure 2(b) are believed to represent regions with real deformation signals (see text).

Figures 2(a) and 2(b) show the interferogram spanning the summer from 14 May 2005 to 27 August 2005 before and after MERIS water vapour correction respectively. This InSAR pair has a small baseline of c. 100 m, and the errors in the SRTM DEM (c. 7.0 m in North America (Farr et al., 2007)) might lead to a phase error of 0.49 rad (i.e. 0.22 cm in the satellite line of sight range changes), which can be considered negligible. The RMS of the unwrapped phase decreased from 1.95 rad before correction to 0.79 rad after applying the MERIS water vapour correction, indicating that the unwrapped phase was much flatter after correction.

In order to validate the MERIS correction model, independent 3D GPS-derived displacements provided by the Scripps Orbit and Permanent Array Center (SOPAC) (Nikolaidis, 2002) were compared with InSAR results in the satellite line of sight (LOS) direction, which showed that the RMS difference decreased from 9.9 mm before correction to 4.1 mm after the MERIS correction.

It is clear in Figure 2(b) that some real geophysical signals were brought out after removing atmospheric water vapour signals: (1) The black dashed oval indicates seasonal surface subsidence in the Long Beach-Santa Ana basin (Argus et al., 2005; Bawden et al., 2001); (2) The white solid oval implies surface subsidence in Antelope Valley (Hoffmann and Zebker, 2003); (3) The black solid circle represents geophysical signals in San Bernardino (Lu and Danskin, 2001).

This case study has two important implications: (1) Water vapour induced range changes in the LOS direction can be greater than 4 cm even in a desert region such as Southern California, and greater water vapour effects are expected in tropic regions; (2) coincident water vapour products are invaluable to assess and then reduce water vapour effects on InSAR measurements. This successful integration of MERIS and ASAR measurements not only contributes directly to the ENVISAT mission, but also will benefit space agencies' plans to design and launch InSAR missions, because intensive investigation of the major error source of InSAR techniques will clearly identify necessary characteristics of future InSAR missions which will in turn aid their ability to better achieve space agencies' science goals.

4. INSAR TIME SERIES WITH WATER VAPOUR CORRECTION (INSAR TS + PWV)

4.1 InSAR time series with water vapour correction

Let t be a vector of SAR acquisition dates in chronological order. For a dataset containing N interferograms constructed from S acquisitions on different dates, assuming $v_{k,k+1}$ is the mean velocity between the time-adjacent (e.g. the kth and $(k+1)th$ time) acquisition, the corrected phase can be written as:

$$\delta\phi_{t_M t_S}^{disp}(x,r) = \frac{4\pi}{\lambda}\Big[d\left(t_S,x,r\right) - d\left(t_M,x,r\right)\Big]$$
$$= \frac{4\pi}{\lambda}\sum_{k=M}^{S-1} v_{k,k+1}\left(t_{k+1}-t_k\right) \tag{3}$$

For a given pixel, let V be a vector (of size $(S-1)\times 1$) of successive velocities (i.e. $V^T = \begin{bmatrix} v_{0,1} & v_{1,2} & \mathrm{L} & v_{S-2,S-1} \end{bmatrix}$), Z a parameter of DEM errors, and R a vector of interferogram range changes in the line of sight (of size $N\times 1$). Equation (2) can be generalized into a matrix equation for the entire set of interferograms:

$$\begin{cases} \begin{bmatrix} T \\ {\scriptstyle N\times(S-1)} & {\scriptstyle N\times 1} \end{bmatrix}\begin{bmatrix} V \\ {\scriptstyle (S-1)\times 1} \\ Z \\ {\scriptstyle 1\times 1} \end{bmatrix} = \begin{bmatrix} R \\ {\scriptstyle N\times 1} \end{bmatrix} \\[2em] C^T = \begin{bmatrix} \dfrac{B_{\perp 1}}{r\sin\theta} & \dfrac{B_{\perp 2}}{r\sin\theta} & \mathrm{L} & \dfrac{B_{\perp N}}{r\sin\theta} \end{bmatrix} \\[2em] R^T = \begin{bmatrix} \dfrac{\lambda}{4\pi}\delta\phi_1^{corr} & \dfrac{\lambda}{4\pi}\delta\phi_2^{corr} & \mathrm{L} & \dfrac{\lambda}{4\pi}\delta\phi_N^{corr} \end{bmatrix} \end{cases} \tag{4}$$

where the $N\times(S-1)$ matrix T references time intervals of each interferogram. If all the acquisitions are well-connected (i.e. they belong to a single sub-network), we should have $N \geq S$, and $A = \begin{bmatrix} T & C \\ {\scriptstyle N\times(S-1)} & {\scriptstyle N\times 1} \end{bmatrix}$ is an S-rank matrix. Therefore, Equation (4) is a well-determined ($N = S$) or an over-determined ($N > S$) system, and its solution can be easily obtained in a least squares sense.

This InSAR time series with water vapour correction (InSAR TS + PWV) technique allows us to map surface deformation as it evolves in time together with a mean velocity field, with two key features: (1) With water vapour correction, no *a priori* deformation model is required in InSAR time series analysis; (2) The capability to provide spatially dense deformation maps is preserved by only using SAR pairs with small baselines. Note that DEM errors are taken into account when using interferograms with a relatively long perpendicular baseline (e.g. >100 m) to increase the amount of data for the time series analysis.

4.2 InSAR time series analyses for postseismic motions after the 2003 bam earthquake

Figure 3 shows 25 ENVISAT images (indicated by red triangles) collected under cloud free conditions in the three years since the 2003 M_w 6.6 Bam (Iran) earthquake, from which 109 interferograms with a perpendicular baseline shorter than 400 m were produced using the JPL/Caltech ROI_PAC software (version 2.3) (Rosen et al., 2004). A subset around Bam (over a 72 km by 72 km area) was unwrapped with the SNAPHU program (Chen and Zebker, 2000).

Two different time series analyses were performed for the 109 unwrapped interferograms: (1) InSAR time series without MERIS water vapour correction. To separate water vapour effects from deformation signals in InSAR time series analysis, an *a priori* temporal deformation model is usually required for most existing InSAR time series approaches (i.e. permanent scatterers and small baseline InSAR) (Raucoules et al., 2007); otherwise atmospheric signals can be estimated by filtering only (Hooper et al., 2007). In this study, no assumption was made for this purpose. (2) InSAR time series with MERIS water vapour correction, as demonstrated in Section 4.1.
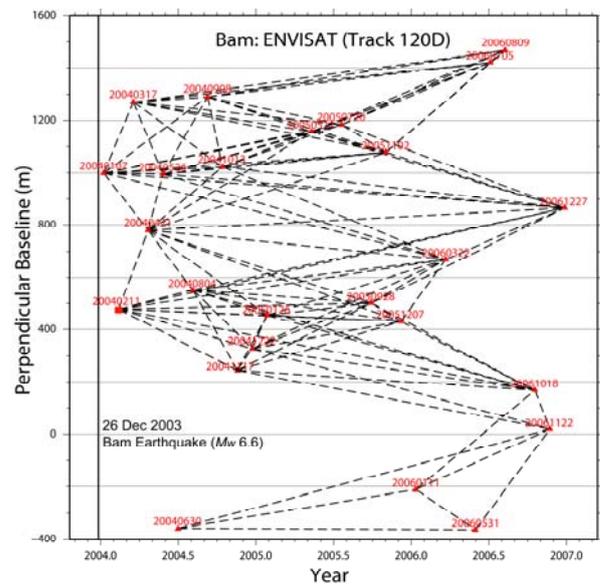
Figure 3. ENVISAT images from descending track 120 (denoted by red triangles with a label of date in format: YYYYMMDD). Black dashed lines connecting triangles represent radar interferograms with a perpendicular baseline shorter than 400 m.

Figures 4(a) and 4(b) show InSAR time series results without and with MERIS water vapour correction respectively on the date of 20041222. It is clear that some phase variations in the Northwest and Northeast corners (indicated by black ovals) in Figure 4(a) were removed and the real geophysical signals (indicated by red open rectangles) were enhanced after correction (Figures 4(b)).
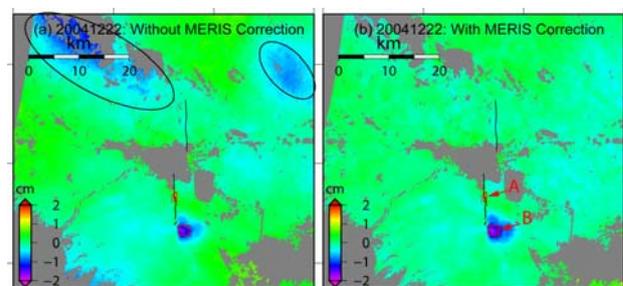
Figure 4. InSAR time series results: the LOS range changes on date: 20041222 (relative to date: 20040211). (a) without MERIS water vapour correction; (b) with MERIS water vapour correction. Note: (1) Thick black lines indicate fault ruptures mapped in the field by Talebian et al. (Talebian et al., 2004); (2)

Black ovals in Figure 4(a) indicate regions with water vapour effects; (3) Positive values imply that the surface moves away from the satellite; that is, the pixel exhibits subsidence in the LOS, e.g. the red open rectangle labelled A; (4) Negative values imply that the surface moves towards the satellite; that is, the pixel exhibits uplift in the LOS, e.g. the red open square labelled B.

Figure 5 shows another example on the date of 20060809. Much stronger phase variations (e.g. those indicated by white ovals) can be observed in Figure 5(a) than Figure 4(a), which were reduced significantly after correction (Figure 5(b)).
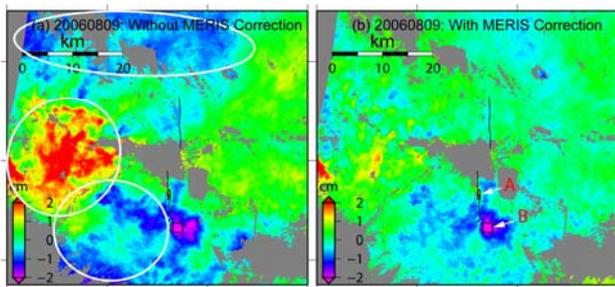
Figure 5. InSAR time series results: the LOS range changes on date: 20060809 (relative to date: 20040211). (a) without MERIS water vapour correction; (b) with MERIS water vapour correction. Panels as in Figures 4(a) – 4(b) except that white ovals indicate regions with water vapour effects in Figure 5(a).

4.3 Three years postseismic motions after the 2003 bam earthquake

The distribution of the postseismic surface deformation indicates that at least two different processes were involved, with different spatial scales and at different depths in the crust (Fielding et al., 2006). A narrow zone (roughly 500 m wide) located where the surface ruptures of the 2003 earthquake were observed south of the city of Bam (open rectangles in Figures 4-5, labelled as A) continued to move away from the descending satellite at least 3 years after the event (not shown in this paper). Since signals with a similar magnitude can be seen on two ascending tracks (156 and 385, not shown in this paper), the displacement must be vertical. This can be interpreted as localized and shallow compaction of material that dilated during the earthquake (Fielding et al., paper in preparation for Science, 2008).

A wider region moving towards the satellite can be observed in the area indicated by open squares in Figures 4-5 (labelled as B), i.e. the east to the south end of the main subsurface coseismic rupture inferred from InSAR measurements (Funning et al., 2005). Since the ascending tracks (156 and 385) show much smaller signals over a smaller area (not shown in this paper), this displacement must include both uplift and eastward components. InSAR time series results reveal that this displacement decays much more rapidly with time than the shallow compaction. The displacement is believed to be due to afterslip above and to the south of the main coseismic slip asperity that ruptured during the 2003 earthquake (Fielding et al., paper in preparation for Science, 2008).

Figure 6 shows that InSAR time series with and without MERIS water vapour correction over Region B (see Figures 4(b) and 5(b)) can be fitted to three different functions:

(1) log(t) function:

$$A + B \times \log(t);$$

(2) exp(t/tao) function:

$$A + B \times \left(1 - e^{t/\tau}\right);$$

and (3) log-exp(P&A) function (Perfettini and Avouac, 2004):

$$S + C \times \log\left(1 + d \times \left(e^{t/\tau} - 1\right)\right),$$

where A, B, S, C, d and τ are constants and t is time in years since the earthquake. Strong variations can be observed in the InSAR time series without MERIS water vapour correction, with a misfit RMS of 0.25 cm. In contrast, the InSAR TS + PWV time series appear to have a smaller misfit RMS of 0.14 cm (i.e. about 50% in reduction). For clarity, only lines showing model fits to the time series with MERIS water vapour correction are plotted in Figure 6. RMS values however are given with respect to their own model fits. Region A (Figures 4(b) and 5(b)) exhibits a similar reduction in the RMS misfit (not shown in this paper).
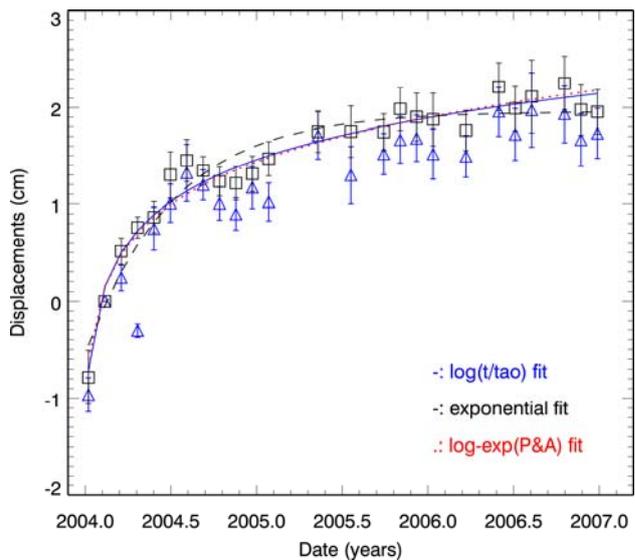
Figure 6. InSAR time series of averages for rapid uplift region B (2 km × 2 km, red and black squares in Figures 4 and 5 respectively). Note: (1) errors were estimated from RMS of the area of interest; (2) Blue triangles represent time series without MERIS water vapour correction whilst black squares indicate time series with MERIS water vapour correction.

5. CONCLUSIONS

InSAR techniques can provide deformation measurements at fine resolution (e.g. tens of metres) over wide areas (e.g. 100 km × 100 km). However, the accuracy of InSAR derived deformation signals is usually limited to centimetre level due to the spatiotemporal variations of atmospheric water vapour. This paper has demonstrated the successful application of MERIS water vapour correction model to ENVISAT ASAR data over southern California: the RMS differences between GPS and

InSAR range changes in the LOS direction decreased from 9.9 mm before correction to 4.1 mm after correction. It is also shown that the integration of InSAR time series and MERIS water vapour correction model (i.e. InSAR TS + PWV) is promising for mapping small deformation signals: (1) it has the ability to map surface deformation as it evolves in time; and (2) it is able to separate deformation signals from water vapour effects without requiring *a priori* deformation model, which is the key advantage of the InSAR TS + PWV approach.

It should be noted that MERIS near IR water vapour products are usable only under cloud-free conditions and 2 ASAR images were excluded in this study due to the presence of clouds. Therefore, the temporal resolution (or sampling rate) of the retrieved deformation time series decreased to some extent, indicating that water vapour data availability is a limitation of the InSAR TS + PWV approach. Since Numerical Weather Models (NWM) can provide estimates of tropospheric path delays with a global coverage, 24 hours a day in all weather, it is likely that the use of NWM will expand the application of the InSAR TS + PWV approach for deformation mapping, which will be an important issue in future work.

REFERENCES

Albert, P., Bennartz, R. and Fischer, J., 2001. Remote Sensing of Atmospheric Water Vapor from Backscattered Sunlight in Cloudy Atmospheres. *Journal of Atmospheric and Oceanic Technology*, 18(6): 865-874.

Argus, D.F., Heflin, M.B., Peltzer, G., Crampé, F. and Webb, F.H., 2005. Interseismic strain accumulation and anthropogenic motion in metropolitan Los Angeles. *Journal of Geophysical Research*, 110(B4): B04401, 10.1029/2003JB002934.

Bawden, G., Thatcher, W., Stein, R., Hudnut, K. and Peltzer, G.,2001. Tectonic contraction across Los Angeles after removal of groundwater pumping effects. *Nature*, 412(23): 812-815.

Bennartz, R. and Fischer, J., 2001. Retrieval of columnar water vapour over land from back-scattered solar radiation using the Medium Resolution Imaging Spectrometer (MERIS). *Remote Sensing of Environment*, 78: 271-280.

Berardino, P., Fornaro, G., Lanari, R. and Sansosti, E., 2002. A new algorithm for surface deformation monitoring based on small baseline differential SAR interferograms. *IEEE Transactions Geoscience and Remote Sensing*, 40: 2375-2383.

Chen, C.W. and Zebker, H.A., 2000. Network approaches to two-dimensional phase unwrapping: intractability and two new algorithms. *Journal of the Optical Society of America A-Optics Image Science and Vision*, 17: 401-414.

Dixon, T.H. et al., 2006. Space geodesy: Subsidence and flooding in New Orleans. *Nature*, 441: 587-588.

ESA, 2004. MERIS Product Handbook, Issue 1.3.

Farr, T.G. et al., 2007. The Shuttle Radar Topography Mission. *Reviews of Geophysics*, 45: RG2004.

Fielding, E.J., Lundgren, P., Li, Z., Funning, G. and Bürgmann, R., 2006. Post-seismic deformation after the 2003 Bam, Iran earthquake from time series analysis of Envisat InSAR, *the 2006 SSA Annual Meeting*, 18-22 Apr 2006, San Francisco, CA.

Fischer, J. and Bennartz, R., 1997. *Retrieval of total water vapour content from MERIS measurements, ESA reference number PO-TN-MEL-GS-005*, ESA-ESTEC, Noordwijk, Netherlands.

Funning, G.J., Parsons, B., Wright, T.J., Jackson, J.A. and Fielding, E.J., 2005. Surface displacements and source parameters of the 2003 Bam (Iran) earthquake from Envisat advanced synthetic aperture radar imagery. *Journal of Geophysical Research*, 110(B9): B09406.

Hanssen, R.F., 2001. *Radar interferometry: data interpretation and error analysis*. Kluwer Academic Publishers, Dordrecht, Netherlands, xviii, 308 pp.

Hoffmann, J. and Zebker, H., 2003. Prospecting for horizontal surface displacements in Antelope Valley, California using satellite radar interferometry. *Journal of Geophysical Research*, 108(F1): 6011.

Hooper, A., Segall, P. and Zebker, H., 2007. Persistent scatterer interferometric synthetic aperture radar for crustal deformation analysis, with application to Volcán Alcedo, Galápagos. *Journal of Geophysical Research*, 112: B07407.

Li, Z., 2004. Production of Regional 1 km × 1 km Water Vapor Fields through the Integration of GPS and MODIS Data, *ION GNSS 2004*, Long Beach, CA, Sep 21-24, pp. 2396 - 2403.

Li, Z., Fielding, E.J., Cross, P. and Muller, J.-P., 2006a. Interferometric synthetic aperture radar atmospheric correction: MEdium Resolution Imaging Spectrometer and Advanced Synthetic Aperture Radar integration. *Geophysical Research Letters*, 33: L06816.

Li, Z. et al., 2006b. Assessment of the potential of MERIS near-infrared water vapour products to correct ASAR interferometric measurements. *International Journal of Remote Sensing*, 27(1-2): 349-365.

Lu, Z. and Danskin, W.R., 2001. InSAR analysis of natural recharge to define structure of a ground-water basin, San Bernardino, California. *Geophysical Research Letters*, 28(13): 2661-2664.

Massonnet, D., Feigl, K., Rossi, M. and Adragna, F., 1994. Radar interferometric mapping of deformation in the year after the Landers earthquake. *Nature*, 369: 227-230.

Massonnet, D. and Feigl, K.L., 1998. Radar interferometry and its application to changes in the earth's surface. *Reviews of Geophysics*, 36(4): 441-500.

Nikolaidis, R., 2002. *Observation of Geodetic and Seismic Deformation with the Global Positioning System*. PhD Thesis, University of California, San Diego, 249 pp.

Panel on Land Subsidence, Committee on Ground Failure Hazards Mitigation Research, Division of Natural Hazard Mitigation, National Research Council, 1991. *Mitigating Losses from Land Subsidence in the United States*. The National Academies Press, Washington, D. C., 68 pp.

Perfettini, H. and Avouac, J.-P., 2004. Postseismic relaxation driven by brittle creep: A possible mechanism to reconcile geodetic measurements and the decay rate of aftershocks,

application to the Chi-Chi earthquake, Taiwan. *Journal of Geophysical Research*, 109: B02304.

Ramon, D., Cazier, L. and Santer, R., 2003. Surface pressure product accuracy with respect to cloud flagging, *Working meeting on MERIS and AATSR Calibration and Geophysical Validation (MAVT-2003)*, ESRIN, Frascati, Italy, 20-24 October 2003.

Raucoules, D. et al., 2007. *Persistent Scatterers Interferometry Independent Validation and Intercomparison of Results – Final Report*, BRGM/RP-55649-FR.

Rosen, P.A., Hensley, S., Peltzer, G. and Simons, M., 2004. Updated Repeat Orbit Interferometry package released. *EOS, TRANSACTIONS, American Geophysical Union*, 85(5): 47.

Talebian, M. et al., 2004. The 2003 Bam (Iran) earthquake: Rupture of a blind strike-slip fault. *Geophysical Research Letters*, 31(11): L11611.

Zebker, H.A., Rosen, P.A. and Hensley, S., 1997. Atmospheric effects in interferometric synthetic aperture radar surface deformation and topographic maps. *Journal of Geophysical Research*, 102(B4): 7547-7563.